



The mechanism of pitting initiation and propagation at deformation bands intersection of cold-rolled metastable stainless steel in acidic ferric chloride solution

Yichong Zhang^{1,2} , Moucheng Li³ , and Hongyun Bi^{2,*} 

¹School of Materials Science and Engineering, Shanghai Jiao Tong University, Shanghai 200240, People's Republic of China

²Shanghai Baosteel Research Institute, Shanghai 200431, People's Republic of China

³Institute of Materials, Shanghai University, Shanghai 200072, People's Republic of China

Received: 25 April 2019

Accepted: 10 August 2019

Published online:

4 September 2019

© Springer Science+Business Media, LLC, part of Springer Nature 2019

ABSTRACT

Pitting initiation and propagation at the deformation bands intersection of cold-rolled 14Cr10Mn stainless steel in acidic ferric chloride solution with a pH of 1.3 were investigated by a scanning electron microscope equipped with electron back scatter diffraction and a high-resolution transmission electron microscopy. The experimental results show that the pits with regular morphology are a sort of dislocation etch pit with strict triggering conditions. The pitting corrosion resistance of the etch pits is closely related to the orientations in the increasing order of $\{100\}\langle 001 \rangle < \{110\}\langle 112 \rangle < \{111\}\langle 110 \rangle$. The pit wall will expand to the periphery along the trend of retaining the close-packed plane, leading to an increase in pit depth after the pitting initiation is triggered. We believe that hydrogen ions compete with chloride ions and preferentially adsorbed on the dislocation outcrops in the austenite around α' -martensite and form hydrogen atoms occupying vacancies to prevent chloride ions from eroding the metal matrix. The results also reveal that the vacancy bands formed by the slip of edge dislocations, and the vacancy groups formed by the dissolve of partial dislocation outcrops are patterns for triggering dislocation etch pits.

Introduction

In recent years, the rapid development of new energy vehicles contributed to the development of the third generation of automotive high-strength steel. Due to the combination of excellent mechanical properties

and corrosion resistance, Cr–Mn–Ni–N series metastable austenitic stainless steel (MASS) can extend the service life of new energy buses from 8 years to 25 years. In particular, the composition design of substituting nickel for manganese allows such stainless steels to be available at a lower price,

Address correspondence to E-mail: hybi@baosteel.com

which has attracted wide attention. Normally, work-hardened state MASSs are applied directly to the products for higher mechanical properties. As a result, the cold-rolled state Cr–Mn–Ni–N series MASSs are widely used in the automobile industry due to their good corrosion resistance and high strength caused by strain-induced α' -martensite transformation [1–3].

As been long-term exposed to the atmosphere, the autobody is affected by several climate factors such as acidic ions and air humidity. Particularly in some coastal cities, chloride ions, and acidic contaminants in moist air will have a significant impact on autobody pitting corrosion. Pitting corrosion is a serious problem for MASS exposed to aggressive environment [4], which is generally considered to be triggered by a combination of internal and external factors such as the impurities, composition, microstructure, environmental chemistry, pH, and temperature [5–9]. To be sure, the internal factor is the main cause in pitting corrosion resistance of materials. Cold working has attracted great attentions due to the introduction of many changes in internal factors, such as deformation bands, which are considered as pitting sources [10, 11]. The experimental results showed that the deformation bands produced by cold working deteriorated the corrosion resistance of nitrogen-bearing type 316L stainless steel, and pits form along the deformation bands in the alloys with 40% cold rolling reduction. It also concluded that dislocation's glide would disrupt the Cr–N short-range ordered zones and form local active electrochemical cells, leading to an increase in pitting sites.

In the present study, interestingly, a type of pits with regular pitting morphology is found in stainless steel, which was initiated mainly at the intersection of deformation bands. Pitting initiation at deformation bands is reported more generally in metallic glass materials [12–14]. However, pitting corrosion in such materials with irregular morphology occurs along the deformation band rather than at the intersection. In addition, pits with regular morphology have reported in monocrystal tin [15], aluminum [16], and some semiconductor materials such as silicon [17], SrTiO₃ [18], CdSiP₂ [19], CdGeAs₂ [20], and silicon steel [21–23]. Such pits are named “dislocation etch-pit,” which, as the name suggests, are usually caused by dislocation outcrops. Different from the pitting behavior of the above materials, the pits with regular morphology of the Cr–Mn–Ni–N MASS mainly occur

at the intersection of deformation bands. As a matter of fact, according to our understanding, there is no definite report on the pitting at deformation bands in MASS. The pitting initiation mechanism is worthwhile aspect with respect to the pitting at the intersection of deformation bands with regular morphology in stainless steels. In this work, a Cr–Mn–Ni–N MASS with plenty of deformation bands was obtained by cold rolling process. The mechanism of the pitting initiation and propagation at deformation bands intersection in acidic FeCl₃ solution is investigated by a scanning electron microscope (SEM) equipped with electron back scatter diffraction (EBSD) and a high-resolution transmission electron microscopy (HRTEM), and the patterns for triggering the pitting are discussed.

Experimental

The experimental material studied in the present work was a Cr–Ni–Mn–N MASS with the name of 14Cr10Mn, which was cast as 30 kg ingot under argon atmosphere at 1250 °C with chemical composition as shown in Table 1. Specimens (size 200 mm × 100 mm × 3 mm) were obtained from the annealed plates under 1180 °C by hot rolling, which pickled by HNO₃ and HF. Subsequently, a unidirectional cold rolling was carried out to reduce the thickness by compression in a laboratory rolling mill at ambient temperature, leading to reductions in final cold rolling by 0%, 5%, and 15% (marked as “CR0,” “CR5,” and “CR15”). At last, 5 mm × 5 mm specimens for ferric chloride solution immersion test and SEM observation were cut by using a wire cutter.

All the chemical immersion test specimens (5 mm × 5 mm) were ground by metallographic sandpapers with grit size up to 2000. Then, use a chemical mechanical polishing slurry containing ultra-fined Al₂O₃ particles to polish all the specimens. An electrochemical etching method was used to remove the surface stress layer of the specimens in 8 vol% of perchloric acid and 92 vol% of ethyl alcohol with an operation voltage of 20.0 V after mechanical ground and polishing. After etching, the specimens were subsequently immersed into a solution of 6 wt% FeCl₃ with 0.05 mol (or 0.01 mol) HCl at 50 °C (shown in Table 2 for details) and then taken out from the solution in every 5 min, till a cumulative total immersing time up to 30 min (or 60 min). Each

Table 1 Chemical composition of the experimental stainless steels (wt%)

Steel	C	N	S	Mn	Si	P	Cr	Ni	Cu	Fe
14Cr10Mn	0.077	0.151	0.0023	10.12	0.30	0.04	13.62	1.19	0.85	Balance

removal was cleaned with deionized water and observed by a scanning electron microscope (SEM, FEI FEG Quanta 600). The crystal orientations corresponding to the pitting initiation positions were performed by EBSD with a scanning electron microscope (FEI FEG Quanta 600, FE-SEM), and the measurements were taken by using an accelerating voltage of 15 kV with step sizes of 0.1 μm . The region of pitting initiation at an intersection of deformation bands after the 30 min cumulative immersion test was selected for observation by a high-resolution transmission electron microscopy (HRTEM, JOEL JEM-2100F). In order to obtain high-quality observation results, the HRTEM specimen was carefully prepared by focused-ion beam (FIB, SMI 3050) method.

Results and discussion

Pits morphology at the intersection of deformation bands

The surface morphology of the immersed specimens was characterized by SEM-BSE to show the deformation bands clearly. Figure 1 shows CR0, CR5, and CR15 specimens of 14Cr10Mn SS after 30 min and 60 min cumulative immersion tests in the acidic ferric chloride solution at 50 °C. For comparison, Fig. 1a exhibits the morphological characteristic of the CR0 specimen after 60 min test in acidic ferric chloride solution with a pH of 1.3. In addition to partial pitting corrosion in the intergranular, no regular morphology pits appeared in grains, indicating that cold deformation is a prerequisite for inducing regular morphology pits. Figure 1b, c exhibits the morphology of pits in single grain and multiple grains of CR5 specimens after the 30 min and 60 min tests in the same solution as CR0. It can be clearly seen that a special type of regular morphology pits, with faceted

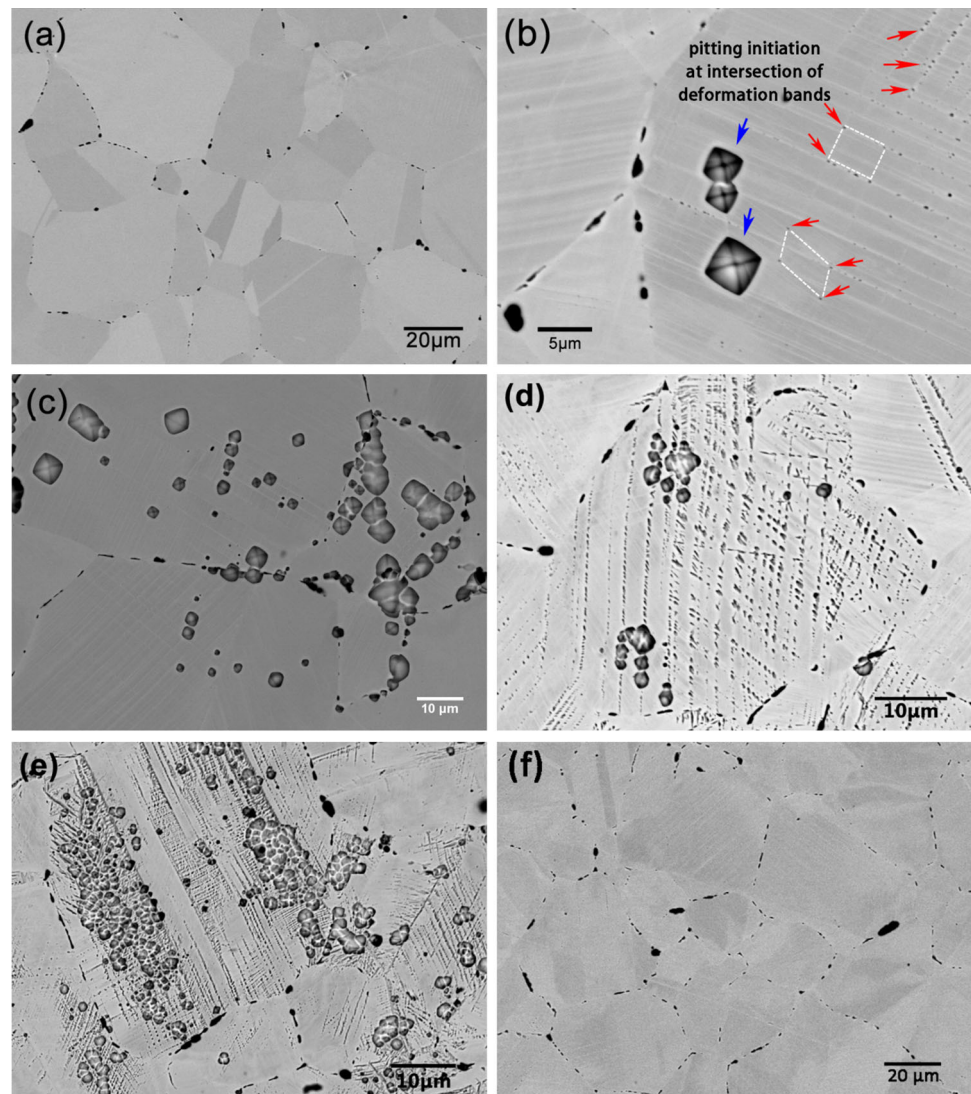
and symmetrical pitting walls, was initiated randomly at the intersection of deformation bands. The number of the pits increased significantly as the immersion time prolongs. Interestingly, unlike the pits shown in Fig. 1a, it can be seen that after the 60 min test in Fig. 1c, there are also some regular morphology pits initiated at the deformation bands around grain boundaries. In addition, the pits have the same structure appearances in the same grain (only differ in sizes), which means that such pits are only related to the orientation of the grain. In order to illustrate the close relationship between the deformation bands intersection and the regular morphology pits, the CR15 specimens were also observed after immersion experiments. Interestingly, similar phenomena occurred in the CR15 specimens after 30 min and 60 min tests in the same solution (shown in Fig. 1d, e). The only difference is that the deformation band intersection density of the CR15 specimen is higher, so is the density of corresponding regular morphology pits, indicating that the regular morphology pits are strongly correlated with the deformation bands intersection. However, no pittings with regular morphology occurred in CR5 specimen in the solution with a pH of 2.0 for 60 min test (Fig. 1f), indicating that the hydrogen ion concentration may be a key factor for triggering etch pits.

Due to the higher deformation band density, the same position of CR15 specimen was selected to investigate the behavior of pitting evolution encountered discontinuous corrosion in the solution of 6 wt% FeCl_3 with 0.05 mol HCl at 50 °C as shown in Fig. 2. For the 5-min immersion test (Fig. 2a), because of the short immersion time, no regular morphology pits appeared at the intersection of deformation bands (see red arrows in Fig. 2a), but only the pits caused by intergranular precipitations can be observed. When the immersion time accumulated to 30 min, pits at deformation bands

Table 2 Different experimental conditions and durations for various specimens

	6 wt% FeCl_3 + 0.05 mol HCl (pH = 1.3)	6 wt% FeCl_3 + 0.01 mol HCl (pH = 2.0)
30 min	CR5 and CR15	–
60 min	CR0, CR5, and CR15	CR5

Figure 1 Pitting morphology at the deformation bands intersections for a 60 min cumulative immersion test of CR0 (a), CR5 (c), and CR15 (e) specimens, and for a 30 min cumulative immersion test of CR5 (b) and CR15 (d) specimen in 6 wt% FeCl₃ with 0.05 mol HCl solution, respectively. f Surface morphology of the CR5 specimen after a 60 min cumulative immersion test in 6 wt% FeCl₃ with 0.01 mol HCl solution. In b, the red arrows point to the pitting initiation at the deformation bands intersections, while the blue ones point to the propagated pits.



intersections began to initiate (see the red dashed circles in Fig. 2b). With the prolongation of the immersion time, more regular morphology pits were formed at the intersection of deformation bands, while such pits still cannot be observed in areas without obvious deformation band structure (Fig. 2c, d).

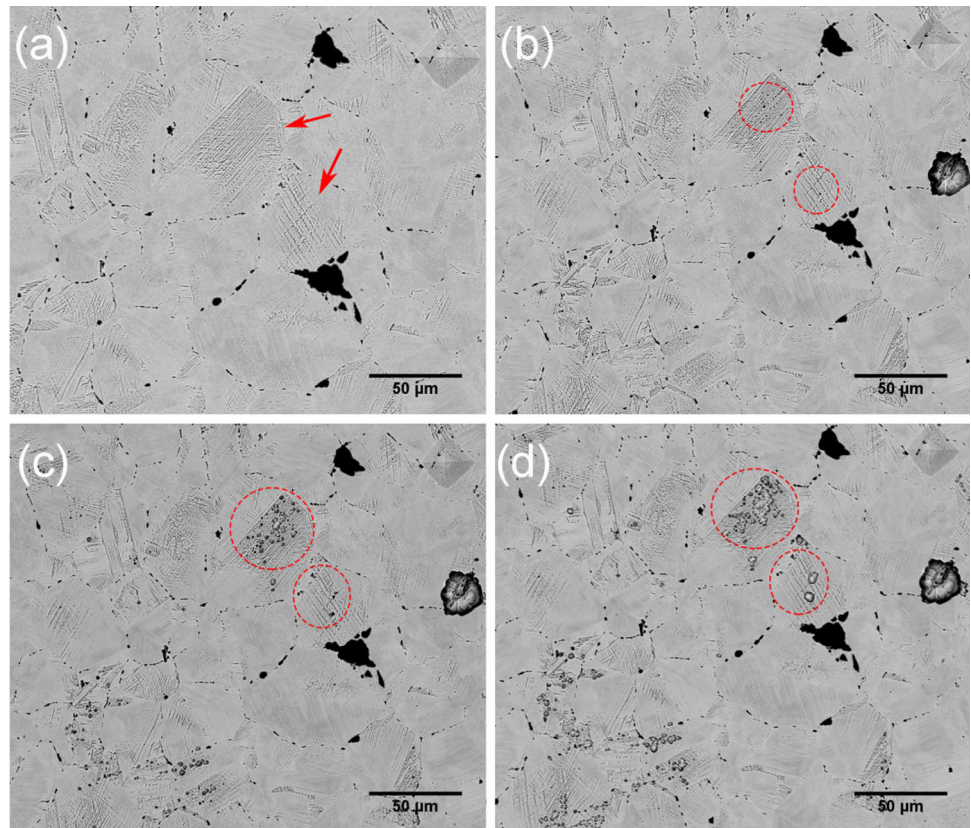
In order to better understand the relationship between grain orientation and pitting at deformation bands intersection, an orientation imaging microscopy (OIM) showed inverse pole figure coloring for the normal direction (ND) of the EBSD method is used to observe pitting corrosion. It should be mentioned that the CR5 specimens are used for EBSD observation in order to obtain a high identification.

Figure 3 displays the orientation imaging microscopy (OIM) for CR5 specimens of 14Cr10Mn MASS

after 60 min immersion test, which have the crystallographic orientations within 15° from {111}⟨110⟩, {110}⟨112⟩, and {100}⟨001⟩ orientations. (The corresponding colors are blue, green, and red, respectively.) In addition, the color shade is inversely proportional to the misorientation, that is, the smaller the misorientation, the darker the corresponding color. It can be observed that the areal fraction of the {111}⟨110⟩ grains is about 21% in Fig. 3a, and the misorientations are mainly less than 10°. It is worth noting that no regular morphology pitting formed and difficult to observe the deformation bands in these grains. In the sketch of grain orientations in Fig. 3b, the red-colored grains occupy an extremely large area. The areal fraction of the {100}⟨001⟩ grains is approximately 37%, but the misorientations are mostly over 10°. Moreover, the {100}⟨001⟩ grains are

Figure 2 A CR15 specimen of 14Cr10Mn SS after 60 min cumulative immersion test in 6 wt% FeCl₃ with 0.05 mol HCl solution at 50 °C.

a 5 min, **b** 30 min, **c** 45 min, and **d** 60 min.



accompanied by a large number of pits at the deformation bands intersection. Figure 3c is still dominated by $\{111\}\langle 110\rangle$ grains, and the misorientations are also mostly over 10° . Fabulously, there is still no pits initiate at deformation bands intersections in these grains. However, in $\{110\}\langle 112\rangle$ grains with similar misorientations, regular morphology pits appeared. The proportions of grains of all three grain orientations in Fig. 3d are no more than 10%, and the misorientations are relatively evenly distributed. However, according to observation, there is still no deformation band etch pit initiation in $\{111\}\langle 110\rangle$ grains, but exists in $\{100\}\langle 001\rangle$ and $\{110\}\langle 112\rangle$ grains. In addition, the deformation band etch pits are present in a large amount in grains having misorientations exceeding 15° from $\{111\}\langle 110\rangle$, $\{110\}\langle 112\rangle$, and $\{100\}\langle 001\rangle$ orientations in Fig. 3a–d. It means that except for the $\{111\}\langle 110\rangle$ orientation, the other orientations are prone to initiate deformation band etch pits.

The EBSD results indicate that the regular morphology pits of 14Cr10Mn MASS formed in acidic ferric chloride solution with the pH of 1.3 are crystallographically dependent. Although all orientations

except $\{111\}\langle 110\rangle$ are prone to initiate deformation band etch pits, according to the number of etch pits, the OIM images also show a tendency of orientations for pitting corrosion resistance to increase in the order of $\{100\}\langle 001\rangle < \{110\}\langle 112\rangle < \{111\}\langle 110\rangle$. In addition, according to the study [16], the index of lattice plane is considered to have a crucial influence on the etch pit. The pitting resistance of different indices of lattice plane shown in Fig. 3 is better supported by the pitting density, that is, the rising trend of pitting density is opposite to that of the pitting resistance. Different from the conclusions by Yasuda et al. [16] and Latanision et al. [24], who suggested that the pitting corrosion resistance order of lattice plane of Al and Ni monocrystals with the same face-centered cubic structure as 14Cr10Mn SS is $\{111\} > \{110\} > \{100\}$. The $\{111\}$ lattice plane as the close-packed plane of the face-centered cubic structure has the best pitting resistance in 14Cr10Mn SS, which is an important result applied to the propagated model of regular morphology pits. Based on this result, we speculate that the pit wall will expand to the periphery along the trend of retaining the

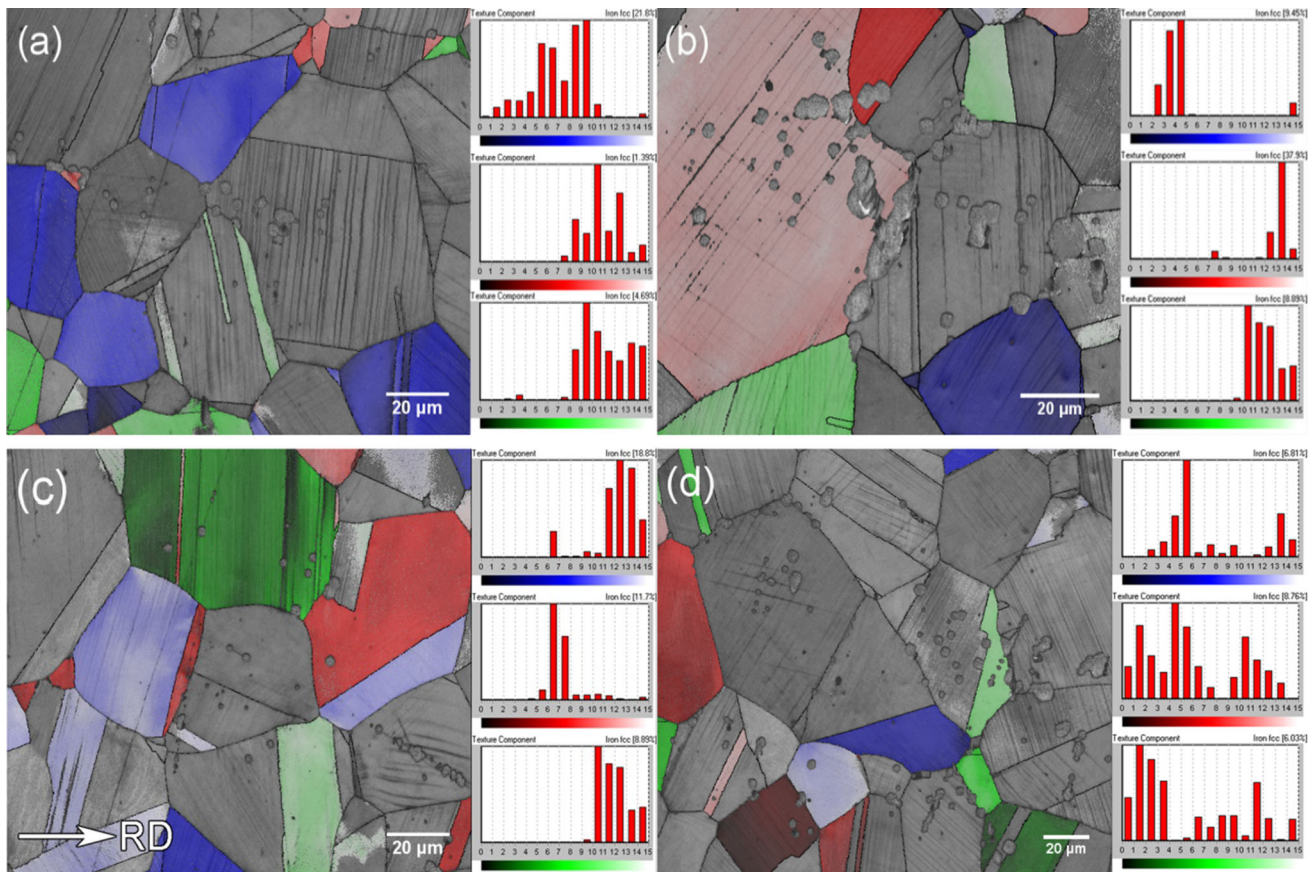


Figure 3 OIM obtained by EBSD showing orientation analysis of the grains of CR5 specimens at the deformation bands intersection (a)–(d) after the 60 min immersion test.

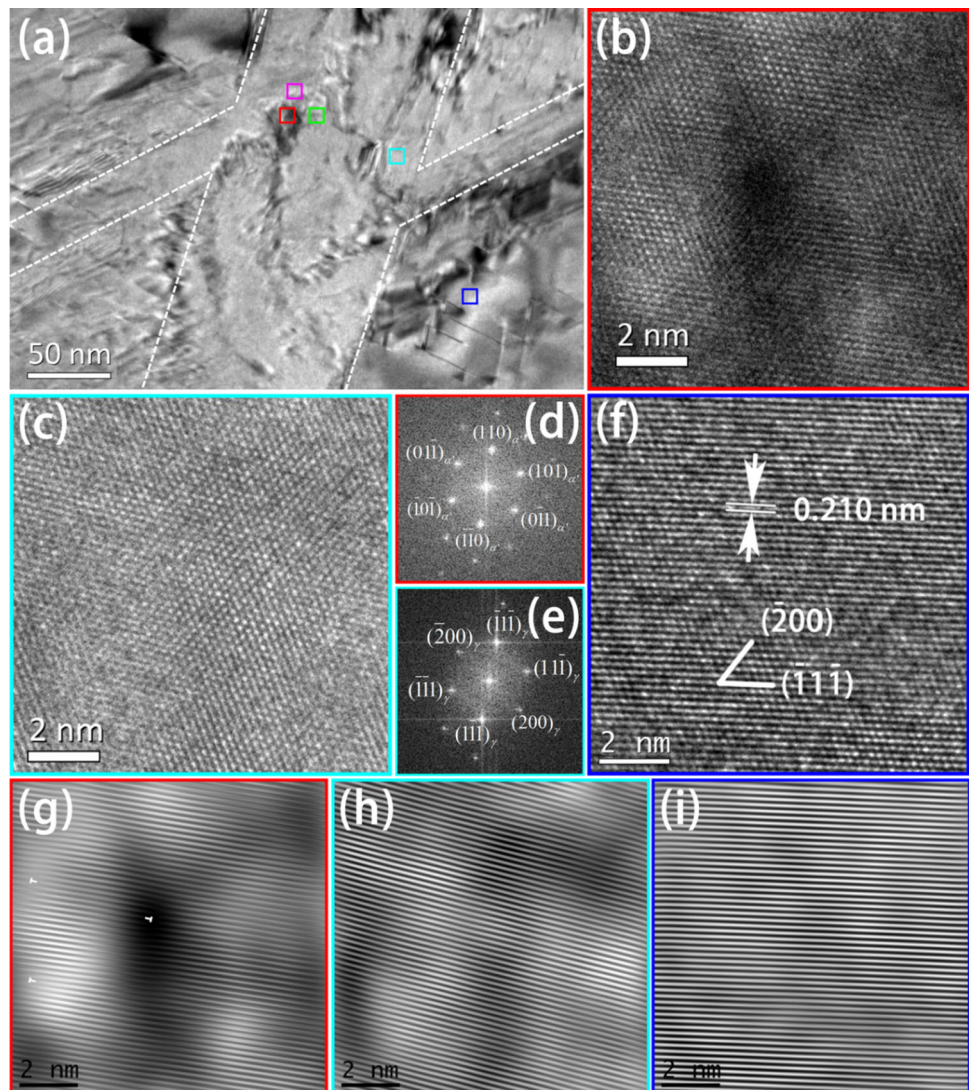
close-packed plane, leading to an increase in pit depth after the pitting initiation is triggered.

Observation of the deformation bands intersection after immersion test

To investigate the pitting initiation in detail, a CR5 specimen immersed in acidic ferric chloride solution with a pH of 1.3 for 30 min was selected; the HRTEM observation on the intersection of deformation bands was performed, and results are shown in Figs. 4 and 5. In Fig. 4a, a well-defined “Z”-shaped kink band appears at the intersection, the edges of which are substantially parallel to the intersected deformation bands. Considering the symmetry of the kink band, parts of the regions were selected for analysis by HRTEM. HRTEM images of the kink band vertex region (Fig. 4b) and the deformation bands intersection region away from the kink band (Fig. 4c) are marked by the red and cyan frame lines in Fig. 4a, obtained along the $[\bar{1}11]$ and $[011]$ axes, respectively.

The fast Fourier transform (FFT) patterns of the regions corresponding to the frame lines in Fig. 4b and c are shown in Fig. 4d, e according to the corresponding colors. It exhibits that the deformation-induced α' -martensite was formed in the vertex region of the kink band, while the other parts of the deformation bands were still austenitic matrix. In addition, the crystallographic orientation of the martensite and austenitic matrix satisfies the K-S relationship, that is, $(\bar{1}1\bar{1})_{\gamma} // (110)_{\alpha'}$ and $[011]_{\gamma} // [\bar{1}11]_{\alpha'}$. Figure 4f shows an HRTEM image of the austenitic matrix outside the deformation band (shown in blue frame lines) for a better comparison of lattice structures in the intersection of deformation bands. An IFFT image with one-dimensional $\{110\}$ plane fringes shows that dislocations can only be observed in negligible quantity in α' -martensite (Fig. 4g). Simultaneously, one-dimensional $\{111\}$ plane fringes images surprisingly revealed that there are almost no dislocations in the austenitic matrix

Figure 4 TEM morphology of the deformation bands intersection in the CR5 specimen after 30 min cumulative immersion test in 6 wt% FeCl₃ with 0.05 mol HCl solution is shown in **a**. HRTEM images along the $[\bar{1}11]$ (**b**) and $[011]$ (**c**) axes show that the deformation-induced α' -martensite is formed in the vertex region of the “Z”-shaped kink band, and the deformation bands remain the austenitic matrix. **d**, **e** The FFT patterns corresponding to **b** and **c**. HRTEM images along the $[011]$ (**f**) axis show the austenitic matrix outside the deformation band. **g–i** The IFFT images clearly show the dislocation structure in the $(\bar{1}\bar{1}\bar{1})$ and (110) planes, respectively.



away from the kink band (Fig. 4h) or outside deformation bands (Fig. 4i).

Figure 5 exhibits the regions immediately adjacent to the vertex of “Z”-shaped kink band (α' -martensite), which corresponds to the green and purple frame lines in Fig. 4a, respectively. An HRTEM image of the area adjacent to the right side of the vertex region obtained along the $[011]$ axes is shown in Fig. 5a, and a structure with an edge dislocation above a vacancy band (marked by elliptical dotted lines in Fig. 5a, c) can be observed. In addition, significant lattice distortions caused by dislocation dipoles and the annihilation process [25] are shown distinctly in Fig. 5c, whereas the matrix is still a face-centered cubic (FCC) austenitic structure (Fig. 5b). Figure 5d shows an HRTEM image of the area adjacent to the upward side of the vertex region obtained along the $[011]$

axes, and two vacancy groups with a dimension of approximately 0.5 nm in diameter formed at the partial dislocation outcrops at both sides of the stacking fault (shown in cyan arrow) are represented by circular dotted lines, combining the one-dimensional $\{200\}$ plane fringes image (Fig. 5f). The above results also show that there is a high density of dislocations in the austenite matrix at the front end of α' -martensite. Furthermore, the distinct lattice distortion regions caused by ion erosion are indicated by red arrows in Fig. 5a, d, which directly cause noise interference of the FFT patterns with the high-density dislocations in Fig. 5b, e.

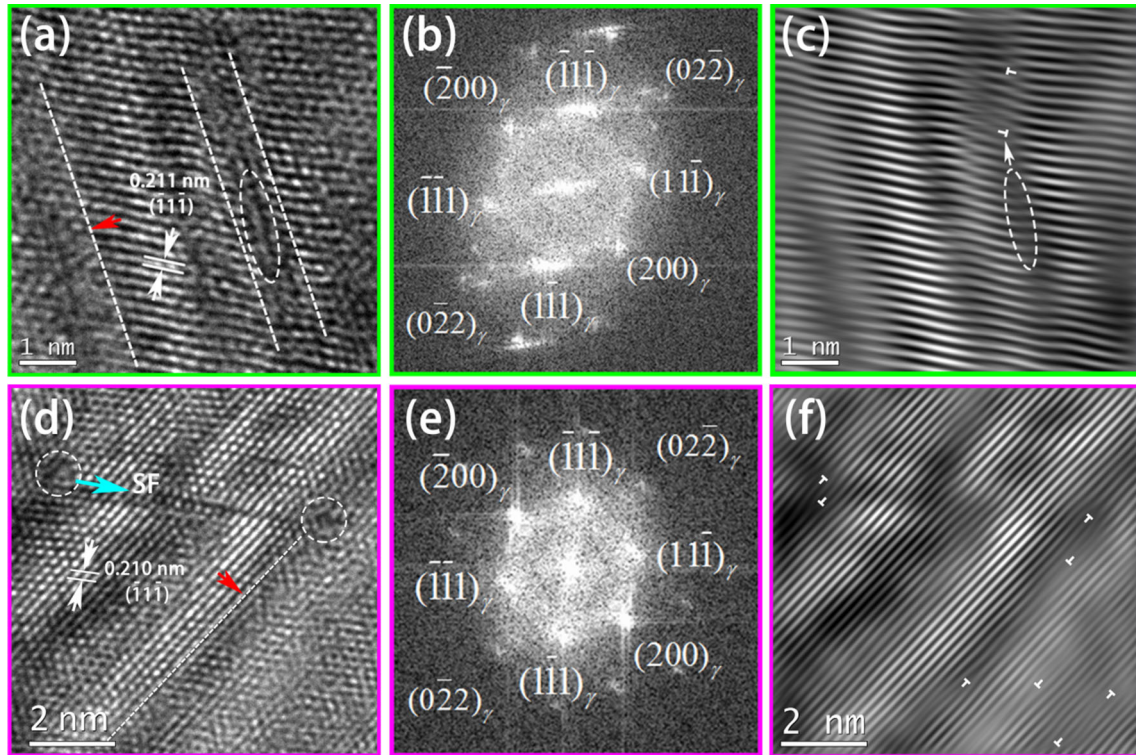


Figure 5 HRTEM images (a) and (d) along the [011] axes show a large number of crystal defects in the austenite matrix at the front end of the austenitic/martensitic hetero-interface after 30 min cumulative immersion test. Apparent lattice distortions caused by corrosion in a and d are indicated by red arrows. The vacancy band in a is indicated by an elliptical dotted line, the vacancy

groups in d are represented by circular dotted lines, and the cyan arrow represents a stacking fault. b, e The FFT patterns corresponding to a and d. Lattice defects cause significant noise interference in the FFT patterns. c, f The IFFT images clearly show the dislocation structures in $(\bar{1}\bar{1}\bar{1})$ and $(\bar{2}00)$ planes, respectively.

Initiation mechanism and trigger patterns of the pits at the intersection of deformation bands

As mentioned earlier, pit with regular morphology called dislocation etch pit is usually caused by dislocation outcrop in FCC structures [15–20]. However, for cold-rolled stainless steel, dislocation outcrops appear randomly on the surface of the specimen due to dislocation pile-up or tangle according to common sense [26] and have been confirmed by our previous work [27] in 14Cr10Mn MASS. It shows that the theory seems not suitable enough for explaining the behavior of pitting initiation at the intersection of deformation bands in MASS as shown in Fig. 1. However, it is worth noting that other FCC materials mentioned above, the same as 14Cr10Mn MASS, also need to form “dislocation pits” under acidic conditions.

In acidic electrolyte, as revealed in Eq. (1), both the major Fe and minor Cr components in metal matrix are selectively dissolved to form metal cations, which are simultaneously hydrolyzed and subsequently deposited [28]. Equation (2) shows hydrogen ions in the solution acquire electrons to form hydrogen atoms. It is worth noting that the tendency of both hydrogen ions and atoms tends to preferentially adsorb at the apparent defect locations with high stress concentration [29].



It has been well reported that α' -martensite is usually generated at intersections of two inclined deformation bands [30, 31]. Dislocations are continuously emitted in front of the austenite/martensite interface due to the high misfit elastic stress, then bowed out and detached from the relatively soft

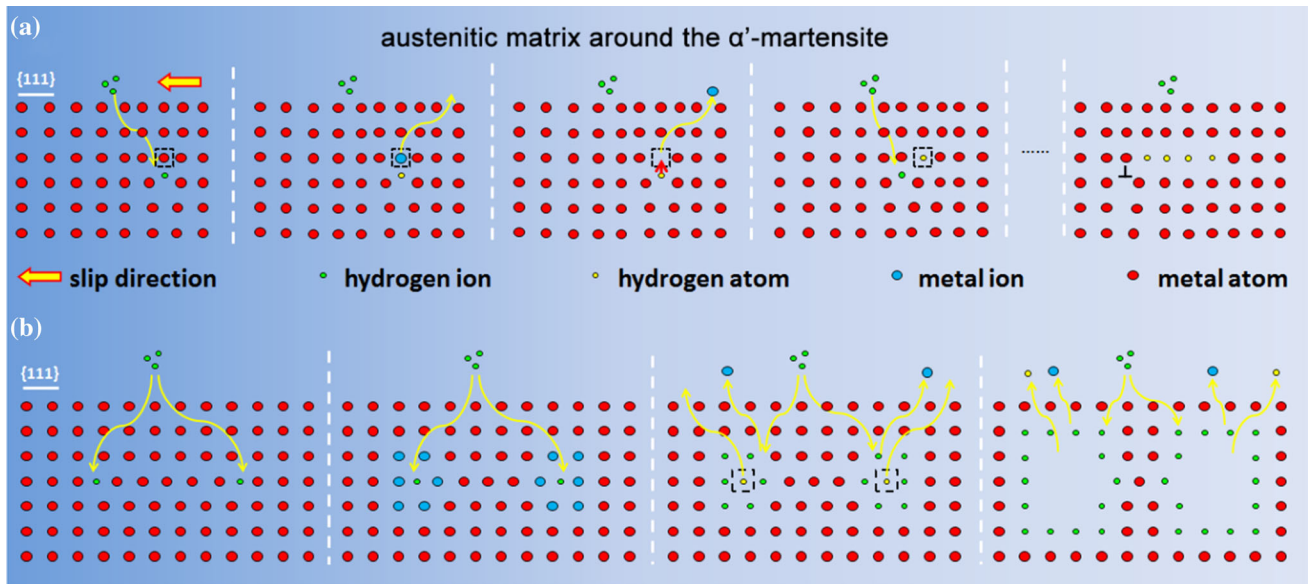


Figure 6 Schematic maps illustrate two patterns of dislocation etch pit triggered by hydrogen ions at the intersection of deformation bands. **a** Hydrogen ions adsorb on the edge dislocation outcrop to form hydrogen atoms and occupy the vacancies, and a vacancy band is formed by dislocation slip.

b Hydrogen ions adsorb on the partial dislocation outcrops on both sides of the stacking fault to form hydrogen atoms. As the pitting propagates, hydrogen atoms that do not adsorb on the metal surface escape and form etch pits.

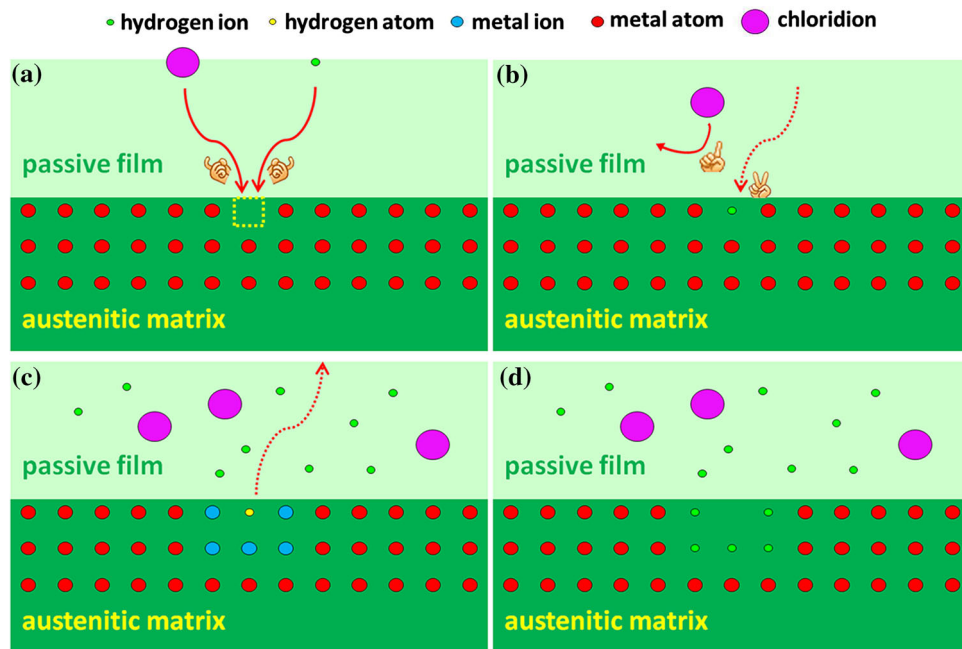


Figure 7 Competitive adsorption model for hydrogen and chloride ions. **a** Hydrogen and chloride ions break into the passive film and produce a tendency to move toward the defect under the influence of dislocation outcrop defects. **b** Compared with chloride ions, hydrogen ions have more adsorption advantages on the high-density dislocation outcrops and prevent

chloride ions from adsorbing on the defects after adsorption. **c** As the corrosion continues, the adsorbed hydrogen ions trap electrons, form hydrogen atoms and escape, and the surrounding metal atoms continue to dissolve along the close-packed plane. **d** Hydrogen ions continue to adsorb along the dissolved close-packed plane, resulting in pitting propagation.

austenitic region during the deformation process [32]. As shown in Figs. 4 and 5, a mass of dislocation structures appears in the austenitic matrix at the front end of the α' -martensite, whereas no significant dislocations in the α' -martensite or the austenite away from deformation bands intersection. The hetero-interface of the austenite/martensite acts as a “dislocation pump,” pumping plenty of dislocations into the austenite matrix around the generated α' -martensite [32], causing a surge in dislocation density, and associating high back stress in the surrounding austenite [33].

Due to the complex dislocation configuration and stress state, the adsorption of hydrogen ions can trigger pitting initiation in several ways. For one, since the metal atoms at the front end of edge dislocation outcrops dissolve, the hydrogen ions adsorb and capture electrons to form hydrogen atoms, subsequently fall into the hydrogen traps formed by the dislocation outcrops. Due to the local stress changes during the dissolution process, the edge dislocation may slip along the close-packed plane. Repeating the above process after slipping will form a vacancy band with several nanometers in length along the dislocation slip direction as shown in Fig. 5a, and the increase in local defects will in turn promote pitting initiation. The above process is distinctly illustrated in Fig. 6a. Another pattern for pitting triggered by hydrogen ions is related to partial dislocation, which is shown in Fig. 5d and illustrated in Fig. 6b. The dissolved partial dislocation outcrops on both sides of the stacking fault are occupied by hydrogen atoms and formed vacancies groups. As the pitting propagation, hydrogen atoms that are not adsorbed on the metal surface escape and form etch pits. This may also be the reason why the surface of the specimen is surrounded by tiny bubbles during the immersion experiment. According to the aforementioned pitting triggering mechanism, it can speculate that the expansion and concentration process of extended dislocations will promote the formation of vacancy groups and accelerate the formation of pits.

There is a variety of theories about hydrogen promoting pitting corrosion initiation. It is generally believed that hydrogen ions enter the passivation film to form hydroxide ions with oxygen ions and then exchange with chlorine ions and cause local enrichment. Or hydrogen ions are enriched around the defects of the passivation film to form a local positive charge region, which causes electrostatic

attraction and enriches the chloride ions at the defects, eventually resulting in pitting initiation [29]. However, these theories cannot explain the difference in morphology between the pit initiated at the deformation bands intersection and those caused by chloride ions in other locations. Since both hydrogen and chloride ions exhibit adsorptivity to defects, combined with the above analysis, a competitive adsorption model for hydrogen and chloride ions is proposed and graphically illustrated in Fig. 7. We believe it may be due to the fact that hydrogen ions are more sensitive to high-stress regions where defects are concentrated than chloride ions. That is, hydrogen and chloride ions have a competitive relationship for adsorption on defect locations, while hydrogen ions have more advantages for adsorption on high-density dislocation outcrops. In particular, hydrogen ions can be adsorbed on an interstitial lattice site at the front end of the dislocation outcrops, while chloride ions are difficult to achieve. The metal atoms at the defect locations lose electrons and dissolve; the hydrogen atoms which formed by trapping electrons are subsequently occupied vacancies, thereby preventing the metal from being attacked by chloride ions. Therefore, only the pits with regular morphology are formed at the region.

Conclusions

A regular morphology pit was found to initiate at the deformation bands intersection of cold-rolled (0%, 5%, and 15% cold rolling reductions) 14Cr10Mn MASS in acidic ferric chloride solution. The following conclusions could be reached:

1. The study has identified that the pit initiate at the deformation bands intersection of the cold-rolled 14Cr10Mn MASS is a sort of dislocation etch pit with strict triggering conditions, which requires high-density dislocations and acidic corrosion condition.
2. The pitting at the deformation bands intersection is related to the orientations, and the pitting corrosion resistance increases in the order of $\{100\}\langle 001\rangle < \{110\}\langle 112\rangle < \{111\}\langle 110\rangle$. When the pitting initiation is triggered, the pit wall will expand to the periphery along the trend of retaining the close-packed plane, leading to an increase in pit depth.

3. By competing with chlorine ions, hydrogen ions are preferentially adsorbed on the high-density dislocations exposed in the austenite at the front of the hetero-interface, capturing the lost electrons from the metal atoms at the defects to form hydrogen atoms, then occupying the vacancies, thereby preventing the attack from chlorine ions. Eventually, dislocation etch pits are formed at deformation band intersections.
4. Two etch pit patterns triggered by hydrogen ions were observed. For one, the hydrogen ions adsorb on the edge dislocation outcrops and form hydrogen atoms to occupy the vacancies which formed by the dissolution of metal atoms. Edge dislocations slip due to the change in the local stress field and form vacancy bands. For another, hydrogen ions adsorb on the partial dislocation outcrops on both sides of the stacking fault, and the formed hydrogen atoms also occupy the vacancies. As the pitting propagates, hydrogen atoms which are not adsorbed on the metal surface will escape and form dislocation etch pits.

Acknowledgements

The authors would like to thank Shanghai Science and Technology Commission Scientific Research Project (15XD1520100) and the National Natural Science Foundation of China (Grant Nos. 51571139 and U1660205) for financial support.

References

- [1] Hariharan K, Balachandran G, Sathyaprasad M (2009) Application of cost-effective stainless steel for automotive components. *Adv Manuf Process* 24:1442–1452
- [2] Kim YH, Kim KY, Lee YD (2004) Nitrogen-alloyed, metastable austenitic stainless steel for automotive structural applications. *Mater Manuf Process* 19:51–59
- [3] Krüger L, Wolf S, Martin U, Martin S, Scheller PR, Jahn A, Weiß A (2010) The influence of martensitic transformation on mechanical properties of cast high alloyed CrMnNi-steel under various strain rates and temperatures. *J Phys Conf Ser* 240:012098
- [4] Lo KH, Shek CH, Lai JKL (2009) Recent developments in stainless steels. *Mater Sci Eng R* 65:39–104
- [5] Sedriks AJ (1979) *Corrosion of stainless steels*. John Wiley and sons, New York
- [6] Frankel GS (1998) Pitting corrosion of metals a review of the critical factors. *J Electrochem Soc* 145:2186–2198
- [7] Sedriks AJ (1986) Effects of alloy composition and microstructure on the passivity of stainless steels. *Corrosion* 42:376–389
- [8] Frankel GS (1998) Pitting corrosion of metals a review of the critical factors. *J Electrochem Soc* 145:675–685
- [9] Schmuki P, Hildebrand H, Friedrich A, Virtanen S (2005) The composition of the boundary region of MnS inclusions in stainless steel and its relevance in triggering pitting corrosion. *Corros Sci* 47:1239–1250
- [10] Ravi KB, Singh R, Mahato B, De PK, Bandyopadhyay NR, Bhattacharya DK (2005) Effect of texture on corrosion behavior of AISI 304L stainless steel. *Mater Charact* 54:141–147
- [11] Mudali UK, Shankar P, Ningshen S, Dayal RK, Khatak HS, Raj B (2002) On the pitting corrosion resistance of nitrogen alloyed cold worked austenitic stainless steels. *Corros Sci* 44:2183–2198
- [12] Pampillo CA (1972) Localized shear deformation in glassy metal. *Scr Met* 6:915–917
- [13] Nie XP, Cao QP, Wu ZF, Ma Y, Wang XD, Ding SQ, Jiang JZ (2012) The pitting corrosion behavior of shear bands in a Zr-based bulk metallic glass. *Scr Mater* 67:376–379
- [14] Wang YM, Zhang C, Liu Y, Chan KC, Liu L (2013) Why does pitting preferentially occur on shear bands in bulk metallic glasses? *Intermetallics* 42:107–111
- [15] Guo R, Tromans D, Weinberg F (1995) Pitting corrosion of passivated β -tin monocrystals. *Corrosion* 51:212–222
- [16] Yasuda M, Weinberg F, Tromans D (1990) Pitting corrosion of Al and Al-Cu single crystals. *J Electrochem Soc* 137:3708–3715
- [17] Borle WN, Bagai RK (1976) Dislocation etch pits on various crystal planes of silicon. *J Cryst Growth* 36:259–262
- [18] Javaid F, Bruder E, Durst K (2017) Indentation size effect and dislocation structure evolution in (001) oriented SrTiO₃ Berkovich indentations: HR-EBSD and etch-pit analysis. *Acta Mater* 139:1–10
- [19] He Z, Zhao B, Zhu S, Chen B, Huang W, Lin L, Feng B (2017) Crystal growth and dislocation etch pits observation of chalcopyrite CdSiP₂. *J Cryst Growth* 481:29–34
- [20] Huang W, Zhao B, Zhu S, He Z, Chen B, Zhen Z, Pu Y (2016) Low-temperature solid-state synthesis and optical properties of CdS–ZnS and ZnS–CdS alloy nanoparticles. *J Alloy Compd* 656:818–824
- [21] Böttcher A, Gerber T, Lücke K (2013) Determination of microtexture of initial stages of secondary recrystallisation in Fe–3 wt% Si by etch pitting. *Mater Sci Technol* 8:16–22

- [22] Inokuti Y, Maeda C, Ito Y (1985) Transmission kossel study of the formation of (110)[001] grains after an intermediate annealing in grain oriented silicon steel containing a small amount of Mo. *Metall Trans A* 16:1613–1623
- [23] Stephenson JD (2010) Some applications of characteristic square etch pits formed on 100 surfaces of Fe–3 wt% Si crystals. *Phys Stat Sol* 39:89–101
- [24] Latanision RM, Oppenhauser H (2013) Passivation of nickel monocrystal surfaces. *Corros Eng* 27:509–515
- [25] Cui JP, Hao YL, Li SJ, Sui ML, Li DX, Yang R (2009) Reversible movement of homogenously nucleated dislocations in a β -titanium alloy. *Phys Rev Lett* 102:045503
- [26] Shen YF, Li XX, Sun X, Wang YD, Zuo L (2012) Twinning and martensite in a 304 austenitic stainless steel. *Mater Sci Eng A* 552:514–522
- [27] Zhang Y, Li M, Bi H, Gu J, Chen D, Chang E, Zhang W (2018) Martensite transformation behavior and mechanical properties of cold-rolled metastable Cr-Mn-Ni-N austenitic stainless steels. *Mater Sci Eng A* 724:411–420
- [28] Zhang B, Wang J, Wu B, Guo XW, Wang YJ, Chen D, Zhang YC, Du K, Oguzie EE, Ma XL (2018) Unmasking chloride attack on the passive film of metals. *Nat Commun* 9:2559
- [29] Qiao LJ (1998) Effects of hydrogen on pitting susceptibility of type 310 stainless steel. *J Chin Soc Corros Protect* 54:628–633
- [30] Olson GB, Cohen M (1975) Kinetics of strain-induced martensitic nucleation. *Metall Trans A* 6:791–795
- [31] Murr LE, Staudhammer KP, Hecker SS (1982) Effects of strain state and strain rate on deformation-induced transformation in 304 stainless steel: part II. Microstructural study. *Metall Trans A* 13:627–635
- [32] Liu J, Chen C, Feng Q, Fang X, Wang H, Feng L, Jian L, Raabe D (2017) Dislocation activities at the martensite phase transformation interface in metastable austenitic stainless steel: an in situ TEM study. *Mater Sci Eng A* 703:236–243
- [33] Somani MC, Juntunen P, Karjalainen LP, Misra RDK, Kyröläinen A (2009) Enhanced mechanical properties through reversion in metastable austenitic stainless steels. *Metall Mater Trans A* 40:729–744

Publisher's Note Springer Nature remains neutral with regard to jurisdictional claims in published maps and institutional affiliations.